

Magnetic Force Imaging of 2D Topological Insulators

Timothy W. Carlson^{1,2}, Swathi Kadaba^{1,2}, Motahhare Mirhosseini^{1,2}, Maria Kolešnik-Gray³, Gabriel Marcus^{1,2}, Lindsey J. Gray^{1,2}, Anthony Walsh^{1,2}, Vojislav Krstić^{1,2,3}, D. L. Carroll^{1,2}

[1] The Nano and Quantum Technologies Laboratory, Wake Forest University, Winston Salem NC 27105, USA

[2] Department of Physics, Wake Forest University, Winston Salem NC 27109, USA

[3] Department of Physics, Friedrich-Alexander-Universität Erlangen-Nürnberg (FAU), Staudtstr. 7, 91058, Erlangen, Germany

Abstract

Two-dimensional topological insulators are central to our understanding of the connection between topological symmetries in a material and its band electronics. Within this class of materials, a breadth of complex quantum behaviors, such as persistent spin-polarized current states in the presence of a broken time reversal symmetry, and temperature-independent topological protection of quantum states, are thought to exist. However, current studies using photoemission and spectroscopic analyses or transport experiments fail to provide insight into the interplay between the physical 2D manifold and the band topology itself, since they do not provide spatial resolution of the phenomena to be understood. In this work, we develop a methodology for applying magnetic force microscopy to such systems to address this issue. Using well-characterized 2D crystallites of bismuth telluride (Bi_2Te_3), we image the magnetic signal directly associated with topological edge states. The observed phase contrast is remarkably robust at a temperature of 25°C and occurs across crystallite sizes and shapes. A detailed analysis of the magnetic imaging suggests that the current observed is composed of two parts: the first is a persistent current ($I_{\text{persistent}}$) as predicted by theory, and the second is due to Faraday induction, I_{Faraday} . Damping dynamics of the cantilever during imaging further suggest that this Faraday *EMF* is established by spin accumulation along the 1D edge channel of the crystal, which then converts to a charge current in the presence of time reversal symmetry breaking, creating a novel form of rectification in the channel. This unexpected result can prompt new ideas for topology-based circuit elements with extremely low losses and power consumption.

Introduction

Topological insulator (TI) systems are of tremendous interest to the condensed matter community because of their immense potential in quantum information technologies^{1,2}. Specifically, applications that may benefit from the robust protections of quantum states offered by complex band topologies include new and novel quantum bit platforms, quantum memories and ultrasensitive quantum sensors³. Across the various topological systems already demonstrated, the most promising are those systems wherein the geometric, real-space topology of the manifold object overlaps in some way with the band topology of that material system as set by spin-orbit coupling and band inversion. 2D TIs are an example of this, where the topology of the bands and the topology of the structure itself can combine to confine specific properties⁴⁻⁶.

A standard for approaching topological states in 2D TI systems is the well-described Kane-Mele model, which exemplifies the Z_2 topological classification with time-reversal symmetry (TRS)⁷⁻⁹. Early experimental evidence in a 2D TI based on mercury telluride (HgTe) quantum wells, as well as an array of studies within the chalcogenide family, have now suggested that spin-polarized topological states are always associated with their D-1 (edge) termination, where D is the dimension of the object. This has become known as the Collins Conjecture¹⁰. Moreover, when the Z_2 symmetry condition is satisfied in the $D = 2$ system (a nanoplate), topological states occur at the edges of those nanoplates.¹¹⁻¹³ In chalcogenide TIs, the materials typically are a small bandgap (0.1-0.3 eV) insulator and these topological states fill the bandgap, making the crystal edge electrically conductive, thus giving the moniker “topological insulator.”

Experimental studies aimed at characterizing TIs have focused on k-space techniques such as angle-resolved photoelectron spectroscopy (ARPES) or two- and four-probe, spin-resolved transport measurements^{14,15}. These approaches form the foundation of our basic understanding of such systems, and they are typically performed at cryogenic temperatures in non-perturbative environments. However, the theoretical expectation for the properties of topological states is their robustness to a wide range of perturbations, including stability against higher temperatures, which other quantum computing platforms, such as Josephson junctions and ion traps, lack¹⁶. Indeed, it is important to note that the temperature behavior of these topological states is directly related to the entropic manifestations of quantum information within such systems¹⁷. Therefore, recent experimental work on topological edge states in the 2D TI Bi_2Te_3 is aimed at understanding protection against backscattering at RT^{14,18,19}. Of particular interest are the characterization and utilization of the unique topological states associated with persistent, nondispersive current flow. These persistent spin-polarized currents occur through TRS breaking in the presence of an applied magnetic field and are predicted to be robust at RT⁹.

Metal chalcogenides can be easily synthesized as layered, 2D crystals with many possessing large spin-orbit coupling and a unique inverted electronic band structure that produces topological features. Extensive research on the synthesis and characterization of colloiddally-grown crystals of these materials has yielded binary, ternary and even quaternary crystallites with a multitude of shapes and applications¹⁹. The versatility in the synthesis of perfect low-dimensional crystals has prompted complementary scanning probe approaches to characterizing their 2D TI properties with high spatial resolution. Specifically, this allows for an examination of the interplay between manifold topology and band topology. Examples of such studies include scanning tunnelling spectroscopy (STS) at cryogenic temperatures, which have shown the presence of a local density of states (LDOS) in the bandgap at the edge of Bi_2Se_3 crystals²⁰. Similarly, Sn and Cd-doped Bi_2Te_3 3D crystals have shown electron oscillations near the cleaved edges

of the crystal²¹ which are proposed to be associated with topological states. These studies are important in demonstrating that the edge of such crystals expresses an enhanced LDOS; however, a direct interpretation of STS-derived LDOS at the edges of materials is challenging since local hybridization can confound deconvolution of the desired signatures²². Moreover, such measurements provide little insight into the robustness of the topological states with increasing thermal fluctuations. Spatially localized optical probes, such as near-field scanning optical microscopy (NSOM), can also be sensitive to spin orientation and local currents using circularly polarized light²³. One such study attributes observed variations in surface charge densities to the existence of screw dislocations and plasmon oscillations in the TI Sb_2Te_3 ²⁴ but does not identify these phenomena with topologically protected states. Overall, the local, real-space probing of the properties of topological states in 2D TIs still faces challenges and gaining insight into their response to changes in thermodynamic conditions is highly non-trivial.

In alternate studies, spin-to-charge conversion in 3D TIs has been explored by probing the electrical current generated on the surface of the TI by the inverse Edelstein effect²⁵. In these experiments, a ferromagnetic layer in contact with the TI is subjected to a static magnetic field and an applied electromagnetic field. The effective vector potential of the magnetized ferromagnet can create a spin accumulation in the TI, which is converted to electric current as a function of the spin relaxation time²⁶. Spin-pumping experiments were further extended to 2D TIs^{27,28}, TIs with magnetic surface impurities²⁹, and on TIs at room temperature¹⁴; however, all of them utilize a ferromagnetic contact under a time-varying electromagnetic field to create the spin imbalance in the TI, with little to no spatial resolution.

In theory, magnetic force microscopy (MFM), which is a contactless probing technique, can be used to obtain a similar process to the above experiments, while also providing spatial contrasts. In this technique, an atomic force microscope (AFM) cantilever is coated with a ferromagnetic material such as cobalt and magnetized, before being brought proximally to within a few nanometers of the TI surface. This establishes a local dipole field. To perform MFM imaging, the tip is dithered near the resonance of the cantilever/tip system, thereby establishing a local time-varying component to the magnetic field. The tip is scanned over the 2D surface of the TI, collecting both a magnetic image and a topographic image. Like the spin-pumping experiments above, the tip induces a local spin imbalance, which in turn produces an electric current that can be probed. For a simple 2D TI crystallite of Bi_2Te_3 , the current magnitude I_{edge} can be approximated by assuming that the current density in the edge channel is given by ev_F where v_F is the Fermi velocity and e the elementary charge. The circumference on which the current flows is roughly πd where d is the approximate diameter of a nanoplate. Taking $d \approx 1 \mu\text{m}$ as typical for our nanoplates, and using a $v_F \approx 10^4 - 10^6 \text{m s}^{-1}$, we find an $I_{edge} \approx ev_F/(\pi d)$ to be in the 1 to 100 nA range^{30,31}. This would lead to magnetic field values easily within the detection limits of most commercial MFMs without the aid of ultra-high vacuum or cryogenic temperatures²⁶. Surprisingly, to date, this avenue of 2D TI study has been left largely unexplored.

In this work, we show that MFM characterization can provide important new insight into 2D TI crystals in temperature ranges not considered previously. Using solution-synthesized micron-sized Bi_2Te_3 nanoplates that are 5-30 quintuple layers thick, we first show that well-formed, perfectly crystalline samples can be produced, which are consistent with other experimental and theoretical studies. Then, electron energy loss spectroscopy (EELS) is used to confirm that these materials exhibit features of topological edge states as identified in the literature.^{32,33} MFM is then used to examine the magnetic fields associated with the system as a function of imaging conditions. From our analysis, we conclude that the magnetic field of an imaging MFM probe creates the TRS breaking needed for a persistent current to exist,

as well as a Faraday induction of current that is generally expected for a metal. This is surprising since such induction is the result of the formation of a back *EMF*, and such an applied *EMF* in the TI typically results in spin currents. Yet, our data seems perfectly consistent with a spin-momentum locked Faraday-induced charge current that is derived from an Edelstein-like mechanism for spin-to-charge conversion. Finally, based on an examination of the limits of the magnetic force gradients observed, we show that the $I_{\text{persistent}}$ magnitude in the Bi₂Te₃ nanoplate system is ~ 802 nA , a value that is close to our naïve expectation.

Discussion of Results

As the sample testbed, the prototypical chalcogenide TI Bi₂Te₃ was chosen and obtained through a hydrothermal synthesis method that has been used extensively in our previous reports.^{34–37} The material system was characterized extensively prior to MFM imaging. The structural analyses of the Bi₂Te₃ nanoplates, as shown in **Figure S2**, confirm a crystalline, stoichiometric material whose lateral dimension is ~ 1 μm and is confined in the vertical dimension to 6-30 nm. As a preliminary check for the observation of spin-selective, electron states that are confined to the edges of the nanocrystal, we also performed valence electron energy loss spectroscopy (**Figure S3**), a method verified specifically for solution-grown chalcogenide crystals.³⁸ Based on the suitability of these Bi₂Te₃ nanoplates, the sample was prepared for MFM imaging as outlined in the methods section.

The MFM scan consists of two steps: the magnetized AFM tip first scans the sample’s surface in tapping mode using the instrument’s feedback to obtain the topographic information of the surface. Then the microscope lifts the magnetic tip above the surface, called the lift height (LH), dithers the tip, and recreates each scanned line using the topographical information to keep the tip at a constant height above the surface. When the tip interacts with any force from the substrate, such as electric and magnetic forces, the phase between the driving force that creates the dithering and the response in the oscillation will shift. The total phase shift is in proportion to the derivative of the force sensed and is given by:³⁹

$$\Delta\phi = -\frac{Q}{k} \left[\left. \frac{dF(x, y, z)}{dz} \right|_{\text{mag}} + \left. \frac{dF(x, y, z)}{dz} \right|_{\text{other}} \right] \quad (1)$$

where k is the cantilever’s effective spring constant, and Q is the quality factor of the cantilever, both at free resonance. $\left. \frac{dF}{dz} \right|_{\text{mag}}$ and $\left. \frac{dF}{dz} \right|_{\text{other}}$ are gradients of the magnetic forces and all other forces, respectively, and z is the distance between the tip and the surface.

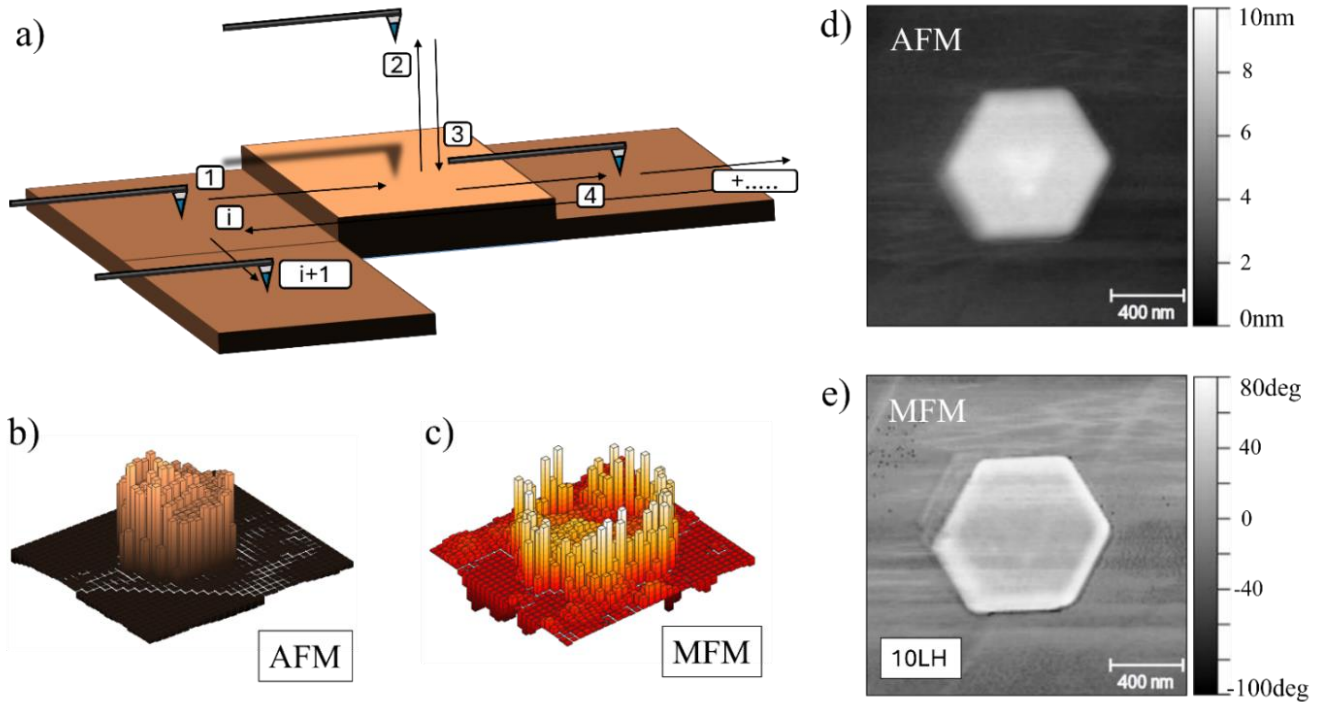


Figure 1: Point-by-point scanning of the scanning probe for MFM. (a) Measurement acquisition schematic. (b) A topographical image (AFM) is shown with a 30 x 30-pixel resolution. The image covers $1.5 \times 1.5 \text{ mm}^2$ over a 600 nm diameter nanoplate. Each column in (b) has a corresponding column in (c), which represents the phase as measured at that location at a 10LH above the nanoplate. (b) and (c) now imaged in 256 x 256 pixels and viewed in 2D, is shown in the image pair (d) and (e). They are, respectively, the topographic image and the phase image or the “MFM image” of the same nanoplate. The imaged nanoplate is 6 nm thick, corresponding to ~ 6 quintuple layers. The nanoplate is supported by highly oriented pyrolytic graphite (HOPG).

There are two common ways of implementing MFM. In the JEOL 5200 SPM system used for these experiments, the cantilever is lifted point-by-point during the scan, as shown in **Figure 1(a)** schematic, and a detailed explanation of the acquisition is presented in the methods section. Thus, the topographic and phase images are interleaved together. Ideally, the same result is obtained from the other common method of lifting the cantilever, which is the line-by-line scan. However, the point-by-point interleaving is chosen over the line-by-line as it is less susceptible to drift when imaging with the cantilever open to the environment. This is possible because the tip height is referenced to the surface morphology at each point of the scan. **Figures 1(b)** and **(c)** show the 3D renderings of the height and phase shift for each acquisition in point-by-point mode. Similarly, **Figures 1(d)** and **(e)** are typical 2D topographic-phase image pairs as collected by the MFM on a 600 nm diameter, 6 nm thick Bi_2Te_3 nanoplate.

In **Figure 1(e)**, we presume that the phase change at the edge of the sample reflects the existence of a magnetic field that is derived from a current that flows around that edge. This isn't surprising since the application of the magnetic field of the MFM tip should break time reversal symmetry for these topological states, and this will theoretically result in a persistent current. Thus, we expect that we are imaging the magnetic field of a constant flowing current that comes along with the topological nature of this 2D Bi_2Te_3 system. There are, however, several excellent models for such imaging^{40,41}, and if we apply any of them

to this image, we can calculate the edge currents but there are nuances to the imaging of topological systems for which we must account.

For instance, we recognize that there is an additional nuance to MFM imaging in this experiment. The magnetic field of the tip can break time-reversal symmetry in the 2D TI, which in turn creates a persistent charge current. That charge current will have a small magnetic field that locally “looks” like that of a wire. Since this current is spin-momentum locked, there is also a magnetic ordering of spins, giving another field arising from aligned magnetic dipoles. Due to the metallic nature of the edge, we further propose that this spin-filtered charge current is obscured by a Faraday induction of *EMF* across the ring, leading to an additional current due to the $d\Phi/dt$ of the tip dither. This is a curious suggestion since it is by no means well established that one can create such a current in the edge channels of a TI through Faraday induction. Moreover, it isn’t clear what the role of the time reversal symmetry breaking might be in such an induced current.

To test this proposed idea, we begin with testing the operational parameters of the cantilever. Typically, mechanisms for contrast in force microscopy are best understood by observing changes in phase as the imaging conditions of height and amplitude of the tip oscillation are varied. If the tip magnetization and cantilever properties are known, optimizing the tip lift height (LH) can determine the steady current sources or magnetic material characteristics. But, when the imaging technique is linked to the creation of the current in the way we have imagined, the link between the height of imaging, the oscillation frequency, the amplitude of the tip and the observed phase is more complicated. For example, when the amplitude of the cantilever oscillation is reduced, the tip will move more slowly through its equilibrium position. This means dB/dt decreases for smaller amplitudes. Thus, the induced *EMF* and consequently the Faraday current will decrease. Moreover, the MFM’s sensitivity to the magnetic field decreases because of the reduced oscillation amplitude⁴². The combination of field change with sensitivity means the effect on phase shifts with cantilever imaging amplitude is amplified. This can be observed in the experiment and can be analyzed by simple models for the tip source system. We apply one such model below with several assumptions about our imaging geometry.

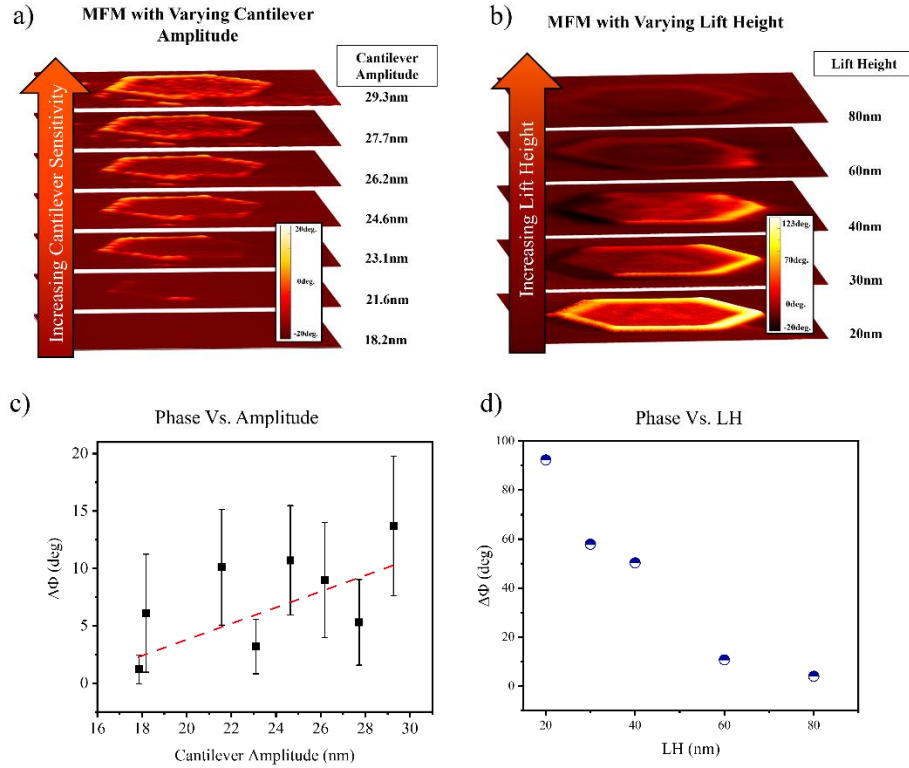


Figure 2: Characterization of the cantilever parameters for MFM. a) Phase shift images at a cantilever LH 100 nm as a function of cantilever oscillation amplitudes. The nanoplate thickness is 20 nm, and the diameter is 1 μm . b) Phase shift variation as a function of LH, keeping the drive amplitude of the cantilever constant at 20.6nm. The nanoplate imaged here is 6 nm thick and 1 μm wide. c) The Df values from the circumference of the nanoplate are averaged to average out leading and trailing edge effects in the scan direction at 100LH, and d) at different LH values. Figures c) and d) are plotted by extracting the values from figures a) and b), respectively.

Figure 2(a) shows the phase shift that occurs for a total change of 2nm in the cantilever oscillator amplitude. This data was taken at LH 100 nm. “Contrast” is the difference in phase between the substrate background and some position on the sample at the same imaging height ($\Delta\phi$). A $\Delta\phi = 1-4^\circ$ becomes apparent only at an oscillation amplitude of 18.9nm, and at an amplitude of 20.6nm, the $\Delta\phi$ is between 25-30° at that same LH. As we have noted, to shift the phase of the resonant oscillation, the field in which the tip is placed must have a gradient. The larger the amplitude of oscillation, the more dF/dz begins to look like a finite difference evaluated at the mean value of the swing amplitude, $\Delta F/\Delta z|_{\text{mean}}$. For a smoothly varying gradient function with no inflection points, this means the phase shift seen by the MFM at larger amplitudes will be larger. If we keep the change in amplitude of the oscillation relatively small, this can be approximated as a linear increase in phase shift with amplitude. Thus, the increase in “sensitivity” is expected to be a linear increase in $\Delta\phi$ with oscillation amplitude under these conditions. To be more precise, the minimum field gradient which can be resolved as a $\Delta\phi$ for a given amplitude of oscillation is the “sensitivity.” As the oscillation amplitude increases, this overall sensitivity increases.

The LH is measured from the bottom of the cantilever's tip swing, so the feedback loop must be active across the scan, and the cantilever must adjust its equilibrium position of oscillation to accommodate the increased swing amplitude. We can estimate the effect of the slight changes in cantilever position from **Figure 2(b)**, where we examine the phase as LH is changed. $\Delta\phi$ shows a predictable decrease as the tip moves away from the surface. Simultaneously, we can conclude that a 2nm shift in the equilibrium position is not large enough to significantly change $\Delta\phi$, although for larger shifts in oscillation amplitude, it might. We expect that this interdependence would lead to a $\Delta\phi$ reduction since the tip would move away from the surface (on average) as the amplitude of oscillation increases. Therefore, from our data, we conclude that for small changes in the amplitude, the effects of feedback and adjustments to cantilever position are second order at best.

In the images of **Figure 2**, we recognize that the phase shift around the perimeter of the sample is not constant, even though we expect the current source that causes this phase shift to be a continuous flow. We note that when imaging isolated samples on a flat substrate, the inhomogeneity of the imaging occurs only in the directions of imaging, that is in the direction in which we scan the cantilever. As we have suggested in our imaging model of the 2D TI the movement of the magnetic tip yields a dB/dt term and this yields an *EMF* across the edge states, which results in currents and magnetic flux gradients. This is a local effect since the phase is taken at the position of symmetry breaking and flux variation from the tip. We therefore expect some variation at the leading and trailing edges of the loop during image generation simply due to Lenz's law. This effect is quantified by varying the scan speed, and this is elaborated in **Figure S4**.

Thus, while we observe a phase shift around the circumference of the TI due to imaging configurations and geometries, it makes analysis of $\Delta\phi$ between imaging amplitudes or lift heights somewhat ambiguous. For very slow scan speeds, if we take the average of the phase shift around the circumference and associate this with the overall induced current into the loop, we might expect the increase and decrease in phase associated with the leading and trailing edges of the tip during the scan to be averaged out. This assumes the primary origin of the imaging artefact is derived from magnetic interactions only. **Figure 2 (c)** and **(d)** show the averaged circumferential phase obtained from the images in **Figure 2 (a)** and **(b)**, as a function of the imaging amplitude and the LH, respectively.

Finally, we note that the two image sets in **Figure 2** are taken on different nanoplates using different cantilevers. While there is a small variation between the tips and thus their sensitivities to the field gradient, we note that the sample in **Figure 2 (a)** is 20 nm thick, and in **Figure 2 (b)** the nanoplate is 6 nm thick. Both are roughly 1 μm in diameter. Normally, we would expect the 20nm thick platelet (20 QL of the Bi_2Te_3) to express 3D TI behavior and currents would be induced in the metallic current states across its surface.⁴³ But in this case, we clearly see edge enhancement associated with a current-derived magnetic field, *i.e.* 2D TI behavior. We suggest that the solution-based synthesis route used to create these nanoplates results in weaker than expected inter-layer interactions, making this stack of 20 QLs behave like 20 2D TIs⁴⁴. If this is the case, then this difference in thickness allows for a difference in current density between the 20 nm thick nanoplate and the smaller 6 nm thin nanoplate. But the same overall current will be induced for a given imaging geometry and drive frequency since the dB/dt term is the same for both systems. Exactly how the current is distributed in the 20 nm stack and in the 6 nm stack isn't clear. So, a direct comparison between nanoplates of different thicknesses can be challenging. However, we would expect to see the difference in 2D and 3D topological behavior by the induced sheet currents that occur in 3D systems.

The $\Delta\phi$ vs. LH in **Figure 2(b)** also allows an indirect examination of the dependence of the electrostatic forces with distance from the surface of the plate. It also shows the dependence of the magnetic component with distance. Ideally, the functional dependence will be different between these two forces, allowing us to separate them. But for this, we will need a reasonable model. Fortunately, there are numerous interaction models for MFM.⁴⁵⁻⁴⁸ In our case, the time-dependent field strength of the dithered dipole on the MFM tip creates the conditions that are ultimately imaged. So, it is most convenient to work at a height that allows us to assume the tip to interact with the nanoplate as a dipole. This reduces the effects of quadrupole and higher moments and makes it easier to model dynamically. Typically, this means LH values greater than or equal to the tip dimensions.⁴⁹ As we will see below, for a $\sim 35\text{nm}$ tip diameter as in our experiments, an LH $> 35\text{nm}$ can reduce the effects of electrostatic interactions due to contact potentials in the microscope. Conversely, a small tip height allows for greater Faraday induction, so a balance must be chosen.

To decouple the components of force in the imaging of the TI system, equation (1) can be written down such that:

$$\Delta\phi = -\frac{Q}{k} \left[\left. \frac{dF_{mag}}{dz} \right|_{mag} + \left. \frac{dF_{elec}}{dz} \right|_{elec} \right] \quad (2)$$

While the origin of the magnetic forces is apparent in the MFM mode of imaging, the electrostatic component arises due to the contact potential in the microscope and acts on the capacitor formed between the HOPG substrate and cantilever + tip. The substrate/tip capacitor has a Bi_2Te_3 dielectric when the tip is over the nanoplate, and no dielectric when the tip is over the HOPG. See **Figure 3**.

Electrostatic Force

The electrostatic forces in the MFM are $F_{electro} \sim F_{VDW} + F_{cap}$, where we include van der Waals and capacitive interactions⁵⁰. After substituting for the two forces (detailed derivation is provided in supplementary information), the final equation we obtain is:

$$\frac{dF_{electro}}{dz} \sim \frac{\pi \epsilon_{\text{BiTe}} R (U_c + U_a)^2 \left[\frac{1}{\epsilon_r} z^2 + 2t_\epsilon z + t_\epsilon^2 \right]}{z^2 (z + t_\epsilon)^2} \quad (3)$$

We define R in equation 3 as the radius of the tip. U_c is the contact potential across the capacitor that is formed between the tip and HOPG. U_a is any additional applied potential. t_ϵ is the thickness of the Bi_2Te_3 nanoplate, and z is the LH. When the tip is very close to the substrate, we can approximate the force gradient over HOPG(BiTe) as:

$$\phi_{elec} = \frac{Q_{\text{HOPG}(\text{BiTe})}}{k} \frac{dF_{electro}}{dz} \sim \frac{Q_{\text{HOPG}(\text{BiTe})}}{k} \frac{\pi \epsilon_{\text{HOPG}(\text{BiTe})} R (U_c + U_a)^2}{z^2} \quad (4)$$

Q , the quality factor of the oscillator will vary over different substrates⁵¹. This approximation can be tested experimentally by examining the $\Delta\phi$ dependence on the applied bias (U_a) as shown in **Figures S10** and **S11**.

Magnetic Force

In our experiments, *MFM01* magnetic tips from *NT-MDT* with an aspect ratio of ~ 430 are used. As noted in the sharp tip ($\sim 35\text{nm}$ dia) approximation, imaging a large plate ($\sim 1\mu\text{m}$ diameter) means the magnetic field appears to the MFM tip as though it comes from a loop of current in which the wires are well separated. The field that the tip experiences at a distance s from the edge current is approximated by Ampère's Law for a straight wire, representing the segment of the loop (the edge of the plate) closest to the tip: $\vec{B}_{edge}(s) \approx \left(\frac{\mu_0}{2\pi} I_{edge}\right) s^{-1} \hat{\phi}$, as shown in **Figure 3 (b)**. This ignores the contributions of the rest of the loop, which is acceptable if the magnetic field of the tip can be approximated as a single effective magnetic moment located along the axis of the tip apex. The relative phase ϕ between the drive voltage and the response of the cantilever, as measured by an MFM in AC mode, derives directly from vertical, lateral, and torsional force gradients applied to the oscillating cantilever system. Generally, the restoring forces in AFM are due to bending modes of the cantilever. But the position-sensitive detector of the AFM used in a normal force AC mode only detects motions along z . So, we are primarily concerned with the restoring forces associated with bends along l (in the x -direction) (**Figure 3 (a)**).

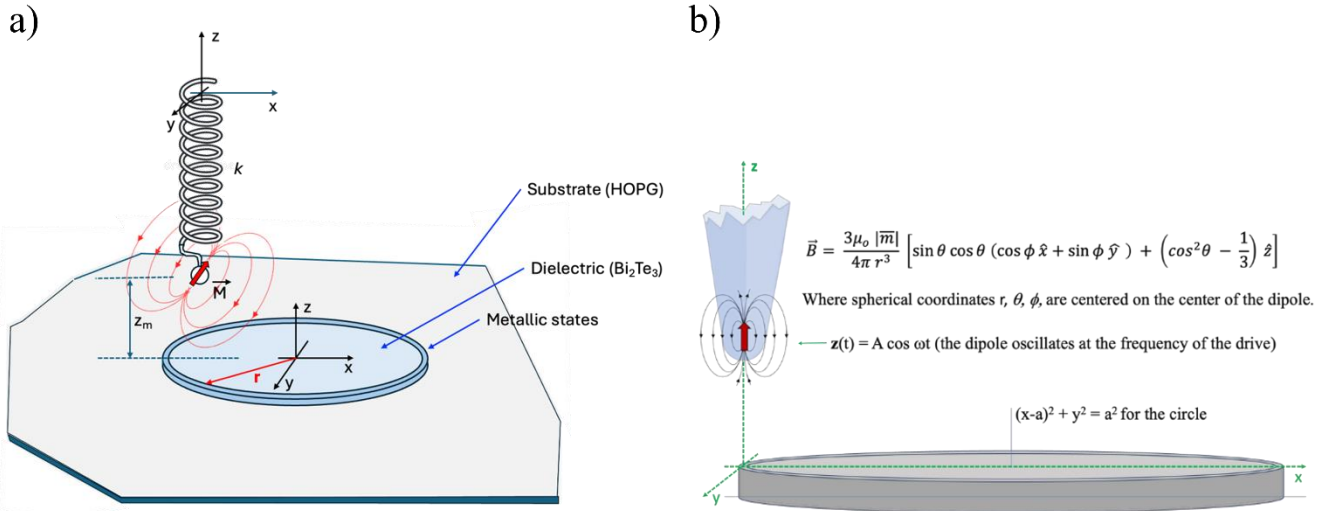


Figure 3: The geometry that we imagine for determining the magnetic and electrostatic field components of the force gradient. a) The capacitor formed below the tip is where the metal support substrate is one electrode, and the semi-spherical metal-coated tip is the other. There are two dielectrics in this system, the air (ϵ_0) and the nanoplate (ϵ_r). The current ring is treated as an isolated wire, wherein the significant interaction comes from the wire segment closest to the tip. b) The tip is a small magnetic dipole, and the current ring is large with a spatially extensive magnetic field. The coordinates of the tip orientation in space are given in spherical coordinates. The nanoplate is described in Cartesian coordinates. Because the cantilever tip is very long in comparison to the z -height, we can treat the dither of the tip as a simple harmonic time-dependent motion in z .

The force on a dipole in a nonuniform magnetic field using the separated magnetic charge model⁵² is given by $\vec{F} = \nabla(\vec{m} \cdot \vec{B})$. By considering the F_z component alone, we can finally obtain:

$$F_z = \frac{\partial(\vec{m} \cdot \vec{B})}{\partial z} = \frac{\mu_0 I m_{eff}}{2\pi} \left[\frac{x^2 - 2xz - z^2}{(x^2 + z^2)^2} \right] \quad (5)$$

Giving a phase shift:

$$\phi = \frac{Q_{edge}}{k} \frac{dF_z}{dz} \sim - \frac{\mu_0 I m_{eff} Q_{edge}}{2\pi k} \left[\frac{1}{z^3} \right]; x = 0 \quad (6)$$

Q_{edge} is the quality factor of the resonator when the tip is positioned far away from the surface. k is the effective spring constant usually provided by the manufacturer, and m_{eff} is the effective dipole moment of the magnetic tip within our dipole approximation⁵². From these expressions, we can experimentally determine $I \sim 79\text{nA}$ for $40\text{ nm} > \text{LH} > 20\text{nm}$ and 1.04 uA for $80\text{ nm} > \text{LH} > 40\text{nm}$ by fitting ϕ vs. $1/z^3$ (as measured at the edge of the nanoplate). This produces current values which change two orders of magnitude with a small change in LH. A possible explanation is that since I is partly an induced quantity, dissipation losses cause the Q factor to reduce. By introducing a damping factor (δ), the damped Q factor is represented as $Q_{l(edge/HOPG)}$ and depends on the resistivity (ρ) of the metal. If we only consider a Faraday current as expected for trivial metals such as gold, we expect cantilever response to follow that of Wakaya et al.⁴² This approach can also be checked for the topological system by estimating what the induced current is from our experiment. We note that the total I is composed of two parts: $I_{persistent} + I_{Faraday}$, and the Faraday current comes from the dithered dipole tip. The Faraday component should minimize as the tip is brought to higher LHs.

To estimate the total I from our dataset, we apply a slight modification of the oscillating dipole model of Wakaya et. al.³⁹ For a dipole placed in the center of the loop of radius r , and oscillating at an equilibrium height z_m above the loop, the flux through the loop is given by:

$$\Phi = \int_0^r B_z^{dipole} 2\pi r' dr' \quad (7)$$

$$B_z^{dipole} = \frac{\mu_0 m_{eff}}{4\pi} \frac{2z_m^2 - r^2}{(z_m^2 + r^2)^{5/2}} \quad (8)$$

However, for a dipole placed at the edge of the loop, the integral can be approximated as $\phi_{Faraday} = \frac{1}{4}\gamma\phi$. This is demonstrated geometrically in **Figure S15**. The factor γ accounts for differences in field density in each area segment. From Faraday, we then get:

$$I = \frac{1}{4} \gamma \left[\frac{3}{4\pi} \frac{\mu_0 m_{eff}}{\rho} \frac{2z_m r}{(z_m^2 + 4r^2)^{5/2}} \dot{z}_m \right] \quad (9)$$

By substituting equation (9) into (6), we obtain:

$$\phi_{Faraday} \sim \frac{3\mu_o^2 m_{eff}^2 C Q_l}{8\pi^3 k} \left[\frac{\dot{z}_m}{z_m^2 (z_m^2 + 4r^2)^{5/2}} \right] \quad (10)$$

$C = 2\pi r/\rho$ (total equivalent conductance of the loop). Given the functional dependence of a dipole field, we take $\gamma \sim 2$ for the circular loop. Combine **Equation 10** with **Equation 6** gives the full expression for the phase from magnetic forces,

$$\phi_{mag} \sim \frac{\mu_0 I_{persistent} m_{eff} Q_{edge}}{\pi k} \left[\frac{1}{z_m^3} \right] + \frac{6\mu_o^2 m_{eff}^2 C Q_{edge}}{16\pi^3 k} \left[\frac{-A\omega}{z_m^2 (z_m^2 + 4r^2)^{5/2}} \right] \quad (11)$$

Where, $z_m = A\cos\omega t + \text{Constant}$ and $\dot{z}_m = -A\omega\sin\omega t$. The phase presented in **Figure 2** is the magnetically derived phase and the electrostatically derived phase added together. The electrostatic (or capacitive) effects yield an attractive force between the MFM tip and substrate as seen in our imaging, too (**Figure S12**). This derives from the whole capacitor, and so it is not as local as our assumptions about the magnetic dipole forces. Thus, they occur at every point of the MFM imaging, and they tend to be averaged effects. The magnetic forces in our induced current loop model repel, and we have assumed that all interactions are with a very small magnetic dipole at the tip's end, so these are local. For a trivial metal, with only the Faraday current contribution, the MFM phase must go to zero as the cantilever amplitude decreases to zero. However, in the topological system there is a persistent current brought on by any static magnetic field. Thus with decreasing amplitude, the phase should decrease linearly as the Faraday component dies away leading to a non-zero y-intercept at zero amplitude. We argue that this reflects that persistent current. Plotting with varying lift heights of phase versus amplitude enables the comparison of several y-intercepts. **Figure 4 (a)** and **Figure S5 (b)** show the phase versus amplitude for three LHs with and without subtraction from HOPG respectively. This distinction is important and is explained in detail in the supplementary information. The quality factor dependence on z can be calculated by setting the y-intercept of **Equation 11** to the data in **Figure S5 (b)** and assume the persistent current is constant at different LHs. From this exercise, the quality factor attains a z^4 dependence. This shows that the previous calculations for the persistent current were based on a wrong assumption. It should be obvious at LHs of 200nm, however, that the Faraday effect on the quality factor is minimized and the original assumption holds. With this noted, the persistent current is now calculated to be 802 nA which is similar to what is predicted theoretically⁴. As shown in Figure 4(a), the lower LHs cross the y-axis at negative values while the 200LH crosses at a positive value indicating the point at which the Faraday component is minimized.

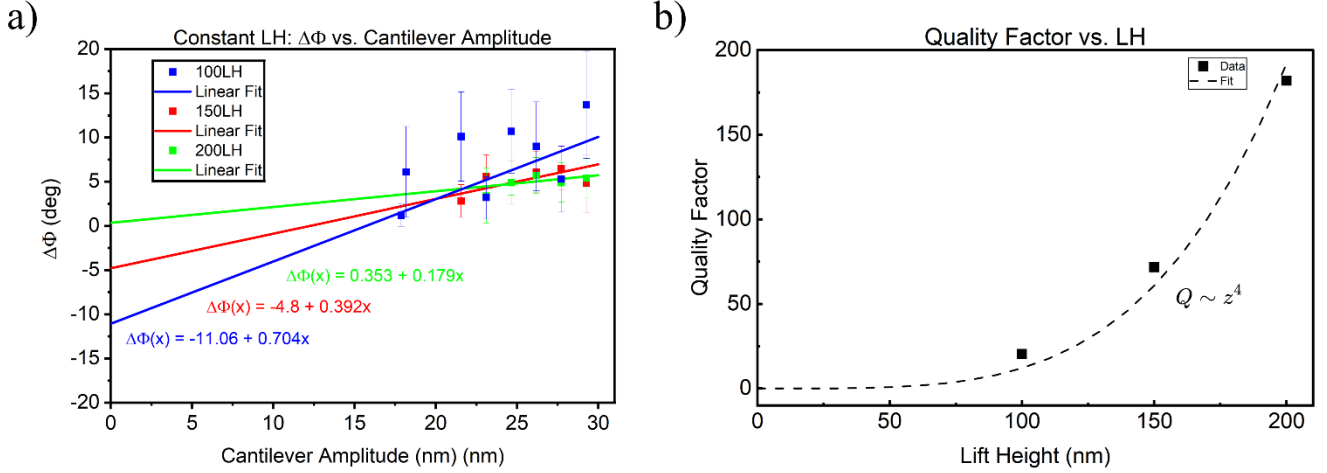


Figure 4: (a) A plot of the phase with amplitude over the edge with lift heights 100LH, 150LH, and 200LH. (b) Plot of lift height versus calculated quality factor with best fit line in dashed.

Discussion of Error

This approach allows us to make some statements about the nature of the topologically protected states by imaging their magnetic properties. But it should be recognized that several approximations were used to make the model calculations simpler, such as the angle of the tip dipole, and the prefactor for the flux-area equation (**Figure S15**). Ultimately, using propagation of errors in the model above, these assumptions can vary the outcome of these results by an estimated factor of $\sim \pm 2\sqrt{2}$. However, they do not represent order of magnitude changes in the predicted values. Further, we have limited these analyses to the dipole interaction approximation. This also makes analytical expressions easier to obtain. We can also make an estimate of the possible error associated with this approximation by making use of a multipole expansion for both the tip magnetic field as well as the source field. In doing so we find that 2nd order corrections for LHs > 35 nm are far more substantial than those at LH ~ 100 nm. Indeed, corrections fall off as $1/z^5$ with the prefactor for the correction being of the same order as the effect at 35 nm. These estimates of error have integrated into the data set presentation as the uncertainty bars on the data points. A final source of error in the analysis comes from the use of the feedback system to adjust the equilibrium position of the cantilever as the amplitude is adjusted. Note that we have written the tip velocities evaluated at the equilibrium positions but have plotted everything as a function of amplitude directly. This introduces an error because the source of the inducing field changes its position in space (its height above the ring) as the amplitude changes. A comparison between small and large amplitude changes is made in the supplementary information **Figure S8**. The effect on the outcome for small amplitude changes is slight ($< 10\%$ in phase).

Conclusion

In this work, we have developed a formalism for the use of magnetic imaging as a method for examining signatures of topological states in TI nanocrystals. Supported by complementary analytical measurements, unambiguous identification of persistent current edge states that are topological in origin has been demonstrated. Such states are robust at room temperature and insensitive to morphological differences in the material system and consistent with the basic assumptions of topological protection. We further find

that even for relatively thick stacks of 2D Bi₂Te₃ nanoplates, the 1D edge current flow indicative of 2D TI behavior survives, suggesting that the solution synthesis method used to create these materials prevents strong interactions between quintuple layers. Finally, the direct imaging of field gradients shows that such currents are associated with a narrow region around the nanoplate edges, which is consistent with multiple theoretical calculations.

The surprising outcome of these studies is the nature of Faraday-like induction of edge currents within the topological system. Generally, it is no surprise that currents can be externally injected into the topological states of a 2D TI. Transport experiments¹⁴ have already suggested this and further suggested that such injected currents are spin-locked with momentum. But those experiments and others like them make use of metal or ferromagnetic contacts, which encounter fabrication challenges and in turn complicates interpretation.^{18,53} In this work, we suggest with some evidence that the mechanism for a $d\Phi/dt$ induced current involves spin accumulation in the edge channel due to an *EMF* being established against the direction of the persistent current. In the presence of the tip dipole field, this is then converted into a current flow, which can be imaged using MFM. This astonishing mechanism for current rectification in a topological conduction channel invites us to consider the possibility of novel circuit elements based on such topological connectivity.

Methods

Atomic/Magnetic Force Microscopy

For the MFM and topographic imaging, HOPG was used as a support substrate due to its atomically smooth surface and homogeneous carrier density.⁵¹ The nanoplates dispersed in ethanol were pipetted onto a freshly cleaved substrate surface. After air drying for 15 minutes, the substrates were imaged in the JEOL 5200, a conventional scanning probe microscope. We obtained a range of thicknesses from 6-30nm (**Figures S1, S7, S8, S12, and S13**). Nanoplate thickness was measured using the non-contact imaging mode. From our X-ray diffraction analyses along with theoretical predictions, a single Bi₂Te₃ quintuple layer (Te1-Bi-Te2-Bi-Te1) is 0.76nm thick⁵⁴ suggesting that the thinnest nanoplates we imaged were ~ 6 quintuple layers.

As shown in **Figure 1 (a)**, the point-by-point MFM mode lifts the cantilever at each pixel of the image. The cantilever moves laterally from pixel to pixel along the AFM scan line using force feedback. However, at each pixel position, the cantilever is raised to a set LH and allowed to dither above the surface through several cycles of the oscillator drive. The phase difference between driving frequency and measured frequency is determined at each of these points and plotted as the “phase image.” The cantilever is then lowered back to the surface, and the AFM feedback is re-engaged. The cantilever then moves laterally to the next pixel location along the scan line, and the process starts over. Detailed methods for extracting the average phase shift values from the phase image are provided in the supplementary information.

References

1. Mercado, M. *et al.* Dynamics of symmetry-protected topological matter on a quantum computer. *Phys. Rev. B* **110**, (2024).
2. Bakshi, A., Liu, A., Moitra, A. & Tang, E. High-Temperature Gibbs States are Unentangled and Efficiently Preparable. *Arxiv* <https://arxiv.org/abs/2403.16850> (2024).
3. Rivas, A. & Huelga, S. F. *Open Quantum Systems*. (Springer Berlin, Heidelberg, 2012). doi:<https://doi.org/10.1007/978-3-642-23354-8>.
4. Michetti, P. & Recher, P. Bound states and persistent currents in topological insulator rings. *Phys. Rev. B* **83**, 125420 (2011).
5. Chen, Q., Li, L. L. & Peeters, F. M. Inner and outer ring states of MoS2 quantum rings: Energy spectrum, charge and spin currents. *Journal of Applied Physics* **125**, 244303 (2019).
6. Qi, X.-L., Hughes, T. L. & Zhang, S.-C. Topological field theory of time-reversal invariant insulators. *Phys. Rev. B* **78**, 195424 (2008).
7. Bernevig, B. A., Hughes, T. L. & Zhang, S.-C. Quantum Spin Hall Effect and Topological Phase Transition in HgTe Quantum Wells. *Science* **314**, (2006).
8. Bernevig, B. A. & Zhang, S.-C. Quantum Spin Hall Effect. *Phys. Rev. Lett.* **96**, 106802 (2006).
9. Kane, C. L. & Mele, E. J. Quantum Spin Hall Effect in Graphene. *Phys. Rev. Lett.* **95**, 226801 (2005).
10. Esquivel, R. O., Rodriguez, A. L., Sagar, R. P., Ho, M. & Smith, V. H. J. Physical interpretation of information entropy: Numerical evidence of the Collins conjecture. *Phys. Rev. A* **54**, (1996).
11. Zhang, Y. *et al.* Crossover of the three-dimensional topological insulator Bi2Se3 to the two-dimensional limit. *Nature Physics* **6**, 584–588 (2010).
12. Shumiya, N. *et al.* Evidence of a room-temperature quantum spin Hall edge state in a higher-order topological insulator. *Nature Materials* **21**, 1111–1115 (2022).
13. Talebi, N. *et al.* Wedge Dyakonov Waves and Dyakonov Plasmons in Topological Insulator Bi2Se3 Probed by Electron Beams. *ACS Nano* **10**, 6417–7224 (2016).
14. Dankert, A., Geurs, J., Kamalakar, M. V., Charpentier, S. & Dash, S. P. Room Temperature Electrical Detection of Spin Polarized Currents in Topological Insulators. *Nano Lett.* **15**, 7976–7981 (2015).
15. Zhang, H. *et al.* Topological insulators in Bi2Se3, Bi2Te3 and Sb2Te3 with a single Dirac cone on the surface. *Nature Phys* **5**, 438–442 (2009).
16. Paszko, D., Rose, D. C., Szymanska, M. H. & Pal, A. Edge Modes and Symmetry-Protected Topological States in Open Quantum Systems. *PRX Quantum* **5**, (2024).
17. Bozkurt, A. M., Kolling, S., Brinkman, A. & Adagideli, I. Entropy driven inductive response of topological insulators. *SciPost Phys.* **8**, (2025).
18. Jamali, M. *et al.* Giant Spin Pumping and Inverse Spin Hall Effect in the Presence of Surface and Bulk Spin–Orbit Coupling of Topological Insulator Bi2Se3. *Nano Lett.* **15**, 7126–7132 (2015).

19. Chen, C. *et al.* Robustness of topological order and formation of quantum well states in topological insulators exposed to ambient environment. *Proceedings of the National Academy of Sciences* **109**, 3694–3698 (2012).
20. Moes, J. R. *et al.* Characterization of the Edge States in Colloidal Bi₂Se₃ Platelets. *Nano Lett.* **24**, 5110–5116 (2024).
21. Alphichshev, Z. *et al.* STM Imaging of Electronic Waves on the Surface of Bi₂Te₃: Topologically Protected Surface States and Hexagonal Warping Effects. *Phys. Rev. Lett.* **104**, (2010).
22. Carroll, D. L. Schottky-barrier formation at nanoscale metal-oxide interfaces. *Phys. Rev. B* **55**, (1997).
23. Kung, H.-H. *et al.* Observation of chiral surface excitons in a topological insulator Bi₂Se₃. *PNAS* **116**, (2019).
24. Hauer, B., Saltzmann, T., Simon, U. & Taubner, T. Solvothermally Synthesized Sb₂Te₃ Platelets Show Unexpected Optical Contrasts in Mid-Infrared Near-Field Scanning Microscopy. *Nano Lett.* **15**, 2787–2793 (2015).
25. Mellnik, A. R. *et al.* Spin-Transfer Torque Generated by a Topological Insulator. *Nature* 449–451 (2014).
26. Wolos, A. *et al.* Landau-Level Spectroscopy of Relativistic Fermions with Low Fermi Velocity in the Bi₂Te₃ Three-Dimensional Topological Insulator. *PhysRevLett.* **109**, (2012).
27. Chen, M. N., Sheng, L., Shen, R., Sheng, D. N. & Xing, D. Y. Spin Chern pumping from the bulk of two-dimensional topological insulators. *Phys. Rev. B* **91**, (2015).
28. Kong, J. *et al.* Quantum spin hall charge pumping characterized by symmetry in 2D topological Sb₂S₃ insulator. *Mat. Tod. Comm.* **36**, (2023).
29. Taguchi, K., Shintani, K. & Tanaka, Y. Spin-Charge Transport Driven by Magnetization Dynamics on the Disordered Surface of Doped Topological Insulators. *Phys. Rev. B* **92**, (2015).
30. Taskin, A. A., Yang, F., Sasaki, S., Segawa, K. & Ando, Y. Topological surface transport in epitaxial SnTe thin films grown on Bi₂Te₃. *Phys. Rev. B* **89**, (2014).
31. Qu, D.-X., Hor, Y. S., Xiong, J., Cava, R. J. & Ong, N. P. Quantum Oscillations and Hall Anomaly of Surface States in the Topological Insulator Bi₂Te₃. *Science* **329**, (2010).
32. La, H. *et al.* Edge-Induced excitations in Bi₂Te₃ from spatially-resolved electron energy-gain spectroscopy. *Ultramicroscopy* **254**, (2023).
33. Lazar, S., Botton, G. A. & Zandbergen, H. W. Enhancement of resolution in core-loss and low-loss spectroscopy in a monochromated microscope. *Ultramicroscopy* **106**, 1091–1103.
34. Dun, C. *et al.* Bi₂Te₃ Plates with Single Nanopore: The Formation of Surface Defects and Self-Repair Growth. *Chem. Mater.* **30**, 1965–1970 (2018).
35. Dun, C. *et al.* 2D Chalcogenide Nanoplate Assemblies for Thermoelectric Applications. *Advanced Materials* **29**, 1700070 (2017).

36. Gray, L. J. *et al.* Solvothermal synthesis of crystalline 2D bismuth telluride with an isoelectronic dopant. *APL Mater.* **12**, (2024).
37. Marcus, G. E., Carlson, T. W., Swathi, K. & Carroll, D. L. Solution-based iron doping of solvothermally grown 2D hexagonal bismuth telluride. *APL Mater.* **12**, (2024).
38. Zhao, M. *et al.* Visible Surface Plasmon Modes in Single Bi₂Te₃ Nanoplate. *Nano Lett.* **15**, 8331–8335 (2015).
39. Sarid, D. *Scanning Force Microscopy: With Applications to Electric, Magnetic, and Atomic Forces.* (Oxford University Press, New York, 1994).
40. Bleszynski-Jayich, A. C. *et al.* Persistent Currents in Normal Metal Rings. *Science* **326**, (2009).
41. Feng, Y. *et al.* Magnetic force microscopy contrast formation and field sensitivity. *Journal of Magnetism and Magnetic Materials* **551**, (2022).
42. Wakaya, F., Oosawa, K., Kajiwara, M., Abo, S. & Takai, M. Detection of nonmagnetic metal thin film using magnetic force microscopy. *Appl. Phys. Lett* **113**, (2018).
43. Kealhofer, D. A., Galletti, L., Schumann, T., Suslov, A. & Stemmer, S. Topological Insulator State and Collapse of the Quantum Hall Effect in a Three-Dimensional Dirac Semimetal Heterojunction. *Phys. Rev. X* **10**, (2020).
44. Chong, S. K. *et al.* Emergent helical edge states in a hybridized three-dimensional topological insulator. *Nature Communications* **13**, (2022).
45. Lohau, J., Kirsch, S., Carl, A., Dumpich, G. & Wassermann, E. F. Quantitative determination of effective dipole and monopole moments of magnetic force microscopy tips. *Journal of Applied Physics* **86**, 3410–3417 (1999).
46. Okamoto, K. *et al.* Resistivity measurement for non-magnetic materials using high-order resonance mode of MFM-cantilever oscillation. *Jpn. J. Appl. Phys.* **64**, (2025).
47. Schaffer, T. E., Radmacher, M. & Proksch, R. Magnetic force gradient mapping. *J. Appl. Phys.* **94**, 6525–6532 (2003).
48. Neves, C. S. *et al.* New insights into the use of magnetic force microscopy to discriminate between magnetic and nonmagnetic nanoparticles. *Nanotechnology* **21**, (2010).
49. Boyer, T. H. The Force on a Magnetic Dipole. *American Journal of Physics* **56**, (1988).
50. Hartmann, U. Magnetic Force Microscopy. *Annu. Rev. Mater. Sci.* 53–87 (1999).
51. Castro Neto, A. H., Guinea, F., Peres, N. M. R., Novoselov, K. S. & Geim, A. K. The electronic properties of graphene. *Rev. Mod. Phys.* **81**, 109–162 (2009).
52. Hartmann, U. The Point Dipole Approximation in Magnetic Force Microscopy. *Phys. Let. A* **137**, 475–478 (1989).
53. Liu, L. *et al.* Spin-polarized tunneling study of spin-momentum locking in topological insulators. *Phys. Rev. B* **91**, 235437 (2015).

54. Li, X., Ren, H. & Luo, Y. Electronic structure of bismuth telluride quasi-two-dimensional crystal: A first principles study. *Applied Physics Letters* **98**, 083113 (2011).